ISSN 0915-633X

INTERNATIONAL ATOMIC ENERGY AGENCY

19 th IAEA Fusion Energy Conference
Lyon, France, 14-19 October 2002

IAEA-CN-94/ TH/6-3

NATIONAL INSTITUTE FOR FUSION SCIENCE

Nonlinear MHD Simulations of Spherical Tokamak and Helical Plasmas

T. Hayashi, N. Mizuguchi, H. Miura, R. Kanno,
N. Nakajima and M. Okamoto

(Received - Oct. 4, 2002)

NIFS-760 Oct. 2002

TOKI, JAPAN

Nonlinear MHD Simulations of Spherical Tokamak and Helical Plasmas

T.Hayashi, N.Mizuguchi, H.Miura, R.Kanno, N.Nakajima, and M.Okamoto

National Institute for Fusion Science, Toki 509-5292, Japan
e-mail contact of main author: hayashi@nifs.ac.jp

Abstract. Nonlinear magnetohydrodynamic (MHD) simulations on relaxation phenomena in a spherical tokamak and a helical plasma, including three-dimensional (3D) equilibrium computations, are executed in full toroidal geometries. For a spherical tokamak, two-step evolution of the medium-n ballooning instabilities and a successive excitation of an internal n=1 crash has been observed. A similar process has been observed in an actual tokamak experiment of TFTR. The process is compared with a previous simulation for another MHD activity that is called the internal reconnection event (IRE). Three dimensional equilibrium code HINT is modified to extend functions, by which an n=1 island structure used for the local island diverter (LID) experiment in the LHD device is analyzed in finite pressure equilibria. Nonlinear simulations are executed for LHD plasma and pressure deformation due to evolution of m=2/n=1 pressure driven mode is observed, which has larger growth rate and saturation level than medium-n ballooning modes.

1. Introduction

We execute MHD simulations to study relaxation phenomena that occur in toroidal plasmas, which are not destructive but spontaneously modify plasma structure such as the pressure profile. In particular, nonlinear dynamics in full toroidal geometries of a spherical tokamak and a helical plasma are studied. The governing equations are a full set of the MHD equations that includes the terms of the resistivity η and the parallel heat conduction κ. The equations are solved by using the fourth-order central-finite-difference scheme and a fourth-order Runge-Kutta scheme.

$$\frac{\partial \rho}{\partial t} = -\nabla \cdot (\rho \boldsymbol{v}), \tag{1}$$

$$\frac{\partial}{\partial t}(\rho \boldsymbol{v}) = -\nabla \cdot (\rho \boldsymbol{v}\boldsymbol{v}) - \nabla p + \boldsymbol{j} \times \boldsymbol{B} + \mu(\nabla^2 \boldsymbol{v} + \frac{1}{3}\nabla(\nabla \cdot \boldsymbol{v})), \tag{2}$$

$$\frac{\partial \boldsymbol{B}}{\partial t} = -\nabla \times \boldsymbol{E}, \tag{3}$$

$$\frac{\partial p}{\partial t} = -\nabla \cdot (p\boldsymbol{v}) - (\gamma - 1)p\nabla \cdot \boldsymbol{v} + (\gamma - 1)(\eta \boldsymbol{j}^2 + \Phi - \nabla \cdot \boldsymbol{q}), \tag{4}$$

$$\boldsymbol{j} = \nabla \times \boldsymbol{B}, \tag{5}$$

$$\boldsymbol{E} = -\boldsymbol{v} \times \boldsymbol{B} + \eta \boldsymbol{j}, \tag{6}$$

$$\Phi = 2\mu(e_{ij}e_{ij} - \frac{1}{3}(\nabla \cdot \boldsymbol{v})^2), \tag{7}$$

$$e_{ij} = \frac{1}{2}(\frac{\partial v_i}{\partial x_j} + \frac{\partial v_j}{\partial x_i}), \tag{8}$$

$$\boldsymbol{q} = -\kappa \nabla_{\parallel}(p/\rho). \tag{9}$$

2. Relaxation Phenomena in Spherical Tokamak

2.1 Simulation Model

The simulation geometry roughly follows the NSTX device. The NSTX device has a conductor shell outside and a rod at the center close to the plasma surface. The computation region covers both the plasma area and the ambient vacuum area which is assumed to be surrounded by perfect conductors. The electron heat conduction is generally large in the direction parallel to the magnetic field in high-temperature plasma. In this paper, we check the effect of such large parallel heat conduction on the dynamics, which is solved with another time intervals, typically several tens of times less than that of the MHD convection terms.

The initial condition is given by an axisymmetric two-dimensional numerical equilibrium which is obtained by the EFIT reconstruction data of the real experiment in NSTX (courtesy of Drs. F. Paoletti, S. Sabbagh, and S. Kaye). The results shown here are derived from the data at 238 msec of the shot #10371, where the central beta is 28%, the central q is 0.89, and the aspect ratio is 1.4. A large scale MHD event was subsequently observed in the experiment. The radial profiles of the pressure, the toroidal current, and the safety factors are shown in Fig.1 (a), and the shape of the plasma is displayed by the contour of the poloidal flux in Fig.1(b). It is noted that the radial profiles are somewhat flat in the core region, compared with the profile for the previous case for the IRE simulation [1].

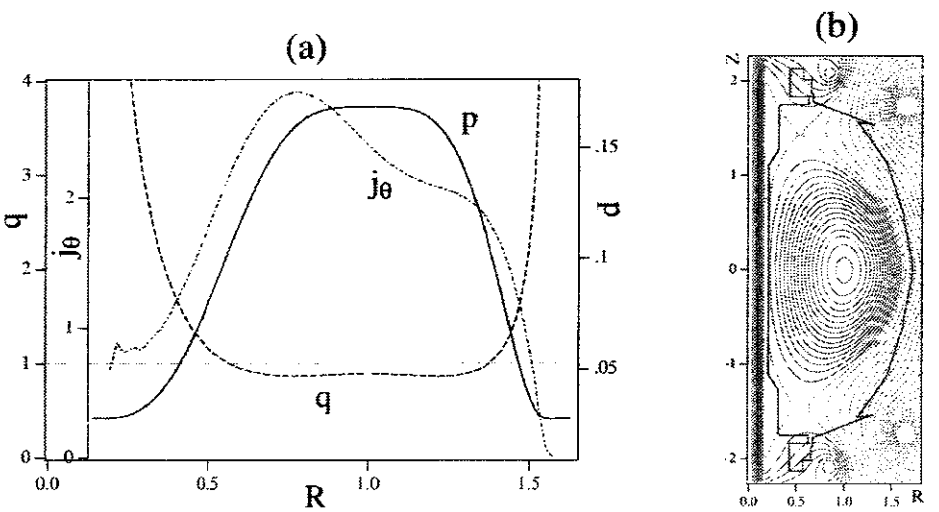

Fig.1 (a)Radial profiles of the pressure, the toroidal current and the safety factor for the initial condition.
(b) Geometry and the magnetic field structure of the initial condition.

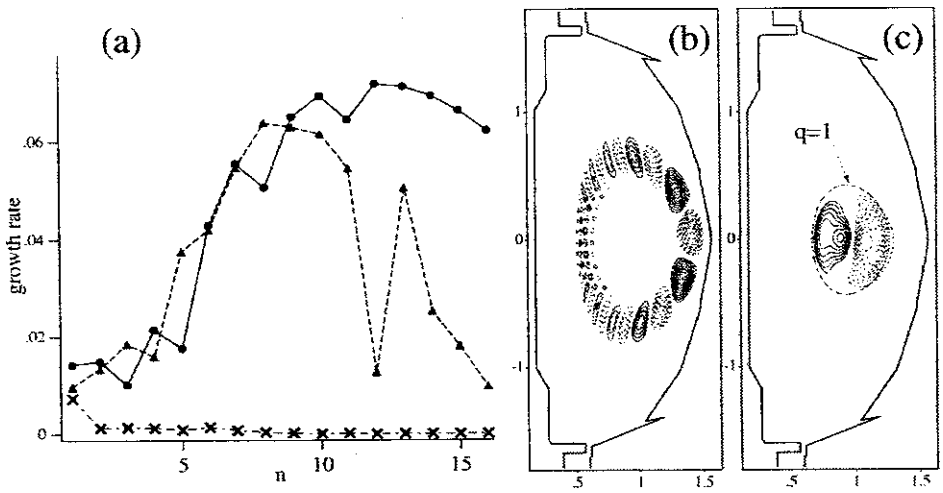

Fig.2 (a) Growth rate of the instabilities for each toroidal modes. The circles, triangles, and the crosses indicate that of the κ=0, κ=4x10^{+0}, and the secondarily induced n=1 mode, respectively. (b)Poloidal mode pattern of the linear n=12 mode for κ=0. The iso-contour of the pressure is plotted. (c)Poloidal mode pattern of the secondarily induced n=1 mode.

2.2 Simulation Results

We calculate the spontaneous time development of the random tiny perturbations given in the initial equilibrium. The initial equilibrium is stable and the perturbations are dumped under the ideal regime, that is, η and κ are substantially small. However, several modes become unstable with larger η. For η=4x10^{-5} (normalized), the most unstable components have medium toroidal mode numbers such as the n=12 and n=13. Shown by the solid circle in Fig.2 (a) is the growth rate for each toroidal mode numbers. The poloidal mode structure is also shown in Fig.2 (b). These resistive modes have the nature of the ballooning modes in that the poloidal mode structures are localized in the bad curvature region. On the other hand, it should be remembered that the lower-n modes is much less unstable in this stage.

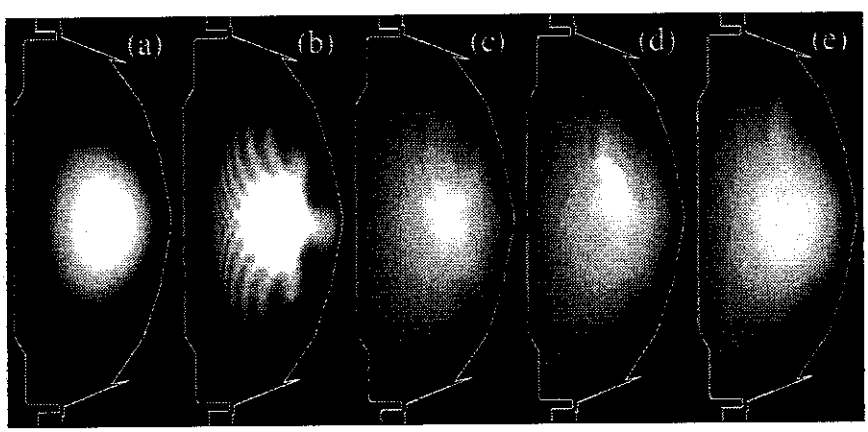

Fig.3 Time development of the poloidal pressure profile for (a)t=0, (b)200, (c)470, (d)550, and (e)760 τ_A.

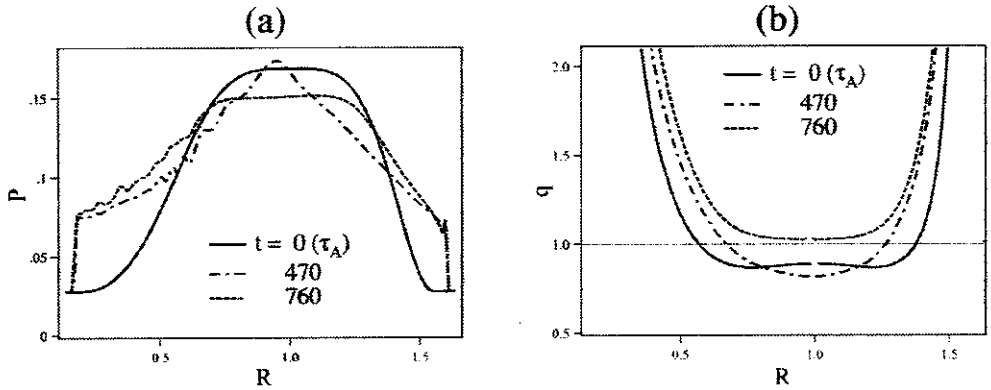

Fig.4 The radial profiles of (a) the pressure and (b) the safety factor for three equilibrium states.

Since the ballooning mode has the parallel component of the wave number to the magnetic field, the growth can be affected by the existence of large heat transport along the magnetic field. We model such heat conduction by adding large parallel thermal conductivity. The symbols with solid triangle in Fig.2(a) indicate the growth rate with normalized $\kappa=2\times10^{+0}$. It can be seen the higher-n ballooning component is suppressed by parallel heat conduction, and the most dominant component is shifted to n=8 in this case.

As the linear unstable modes grow, the amplitude of the perturbation becomes so large that the distortion in global structure becomes visible scale. Shown in Fig.3 is the time evolution of the poloidal pressure profile. The plasma surface wrinkles at the periphery region due to the ballooning modes (Fig.3 (b)). Then the pressure collapses in the periphery, but the high pressure region still remains at the core region (Fig.3(c)). In this state, the total kinetic energy of the plasma decreases to a minimum state, that is, the system is relaxed to a new equilibrium state. The temporal changes in the radial pressure and safety factor profile are shown in Fig.4. The new relaxed state is indicated with dash-dotted line. One can see that the pressure profile becomes more peaked since the peripheral structure collapses by the ballooning modes. The safety factor, on the other hand, also has the region below unity, the system still has instability.

About 200 Alfven transit time later, as is shown in Fig. 3(d), another large-scale instability begins to grow. This mode has the m/n = 1/1 component dominantly. The poloidal mode structure of the n=1 mode is plotted in Fig.2(c). The perturbations consist of a pair of positive and negative pressure fluctuations, and exist widely inside the q=1 rational surface. Another analysis by using the energy principle shows that the source of energy to drive the instability comes from the current-driven term. These observation proves that the secondarily induced instability is an n=1 internal kink mode. The central hot plasma region is largely shifted from the core to the edge, and is split in two fractions in the poloidal cross section near the q=1 rational surface, and the plasma convection motions lead the hot plasma to the core region again. The system relaxes to an axial equilibrium again (Fig. 3(e)). The radial pressure profile in this state becomes a broader one again (Fig. 4(a)), and the region where the safety factor below one vanishes (Fig. 4(b)).

2.3 Discussions on Spherical Tokamak Simulations

The simulation result described above shows some unique features. The sawtooth-like n=1 crash is induced as a result of the spontaneous time development of the middle-n ballooning precursors in our simulation. Such two-step evolution of the medium-n ballooning instabilities and a low-n crash has been observed experimentally in TFTR [2]. In the TFTR case, after the middle-n ($4<n<10$) ballooning activities are observed, an internal beta collapse accompanied by an m/n=1/1 components occurs, and the electron temperature decreased in the core region. This observation is comparable with our simulation results in the mode structures of the related instabilities.

In spherical tokamaks, the n=1 activities are often observed as the Reconnection Events and as the ordinary sawteeth (internal n=1 activities) when the central q goes below one. It is meaningful for us to compare the REs and sawteeth from the point of view of nonlinear simulations. Our previous simulation [1] models the Internal Reconnection Event observed in START. Experimentally, these phenomena have several common features such as a large scale pressure collapse (IRE or RE) and an n=1 fluctuation of the precursors. However, the IRE can be distinguished from the sawtooth in that the plasma global shape is largely distorted and the stored heat energy is lost. The IRE simulation results reproduce the large distortion and related activities on an IRE. These activities are induced by the magnetic reconnection between the internal and external field, which occurs by formation of a large and localized pressure bulge on the torus surface due to the growth of the combination of the m/n=1/1 and 2/2 interchange modes. Significant amount of the plasma pressure energy is lost from the reconnection point, and the overall shape of the torus becomes largely twisted by the strong plasma jet flows excited along the reconnected field lines. Thus, it is shown that the differences on the nonlinear time development between the sawtooth and the IRE case arise from only slight discrepancies in the initial profiles. Though the detailed mechanism is not clear yet, it is revealed by the simulation that the difference between linear instability modes can change the nonlinear time development, i.e., the internal kink induced by ballooning leads the internal n=1 activities, and the interchanges lead the RE.

3. Nonlinear Evolution of Pressure-driven Instabilities in a Helical System

3.1 Extension of the HINT code

The 3D equilibrium code HINT, which does not assume the existence of magnetic surfaces, is modified in a couple of directions to extend the functions [3]. (a) Coil currents can exist in the computation region. (b) The net toroidal current effects (Ohmic and Neoclassical) are consistently treated in the evaluation of the island formation. (c) The full torus configuration is consistently treated [4]. Thus, the usefulness of the code is largely enhanced.

Owing to the modification (c) of the code, behavior of magnetic islands that do not keep the stellarator symmetry can now be treated for a finite beta equilibrium. The m/n=1/1 island structure that is used in the local island divertor (LID) experiment in Large Helical Device (LHD) (ref. [5]) is such an example, as is shown in Fig.5.

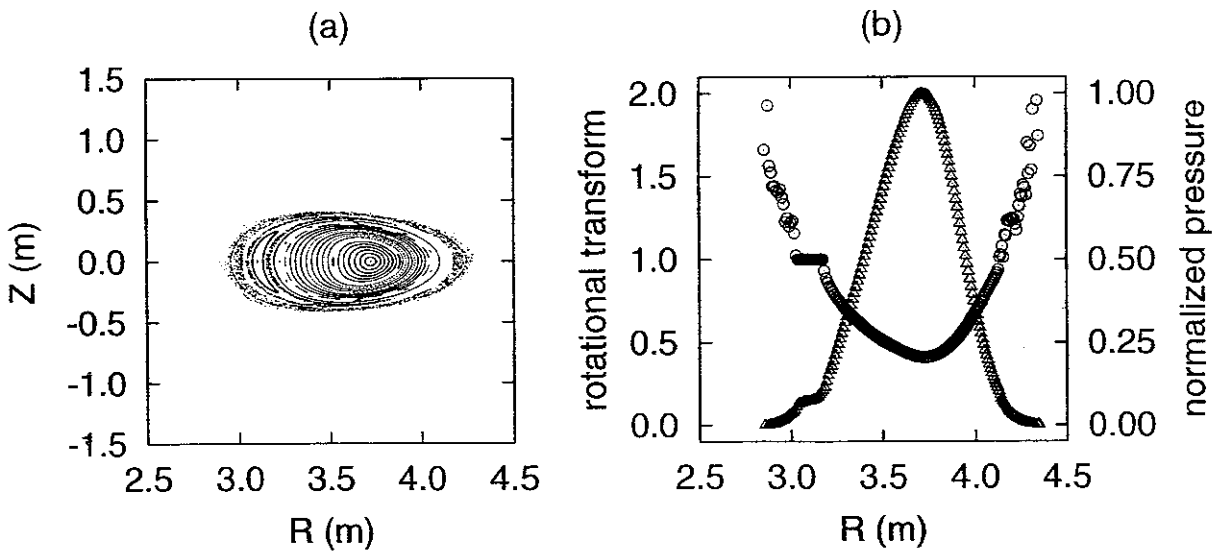

Fig.5 (a) Poincare plots of field lines at the horizontally elongated poloidal cross section and (b) profiles of rotational transform (open circle) and pressure (open triangle) at Z=0 in the horizontally elongated poloidal cross section in a LHD equilibrium with the m/n=1/1 island for beta=2%.

3.2 Simulation Model and Results

Based on a HINT equilibrium, nonlinear evolution of pressure-driven instabilities is studied in a full 3D geometry of LHD (Large Helical Device), which has seldom been attempted. We solve the MHD equations described in the helical-toroidal HINT coordinate system. The number of the grid points is 97x97 on a poloidal section and 640 in the toroidal direction. The kinetic viscosity and the heat diffusion coefficient are fixed as $2.x10^{-2}$ and $1.x10^{-6}$, respectively. Two simulations with the resistivity $1.x10^{-6}$ and $5.16x10^{-6}$ are conducted. We refer to the former (latter) resistivity as the lower (higher) resistivity. We also conduct nonlinear simulations of the half-pitch period system under the stellarator symmetry in order to compare the results with full-torus simulations. The initial equilibrium has the initial position of the vacuum magnetic axis R_{ax}=3.6m for the actual LHD device and the initial central beta $\beta(0)$=4%.

In Fig.6, time evolutions of the kinetic energy per unit volume are shown. The solid lines represent runs with the higher resistivity while the dashed ones represent runs with the lower resistivity. Thick lines are for full-torus runs and thin lines are for half-pitch simulations. We find that the full-torus runs attain higher saturation levels than their half-pitch counterparts. Because of the rapid growth of the kinetic energies in the full-torus simulations than in half-pitch simulations, low toroidal (n) modes are dominant from the initial phase of the growth. However, detailed observations reveal that the smaller poloidal modes (m) are significant in the mid of the energy growth, which are the medium-wave number ballooning instabilities (Miura et al[6]), though the figures are not shown here.

The ballooning instability is saturated due to the nonlinearity of the MHD equation. At the saturation time, a distinct m/n=2/1 structures are observed in the isosurface of the pressure in Fig.7. The mode structures are clearly different from the ridge-like structure formed in the pressure profile that has been

observed in the half-pitch simulations [6].

In order to see how the m/n=2/1 structures are formed, we have observed time-sequence of the pressure on a horizontally- and vertically-elongated poloidal sections. In Fig. 8, color contours of the pressure on a horizontally-elongated poloidal section are shown with the streamlines as a typical example. The black ellipses represent the magnetic surfaces with the rotational transform 1/2 (the inner ellipse) and 2/3 (the outer ellipse).While the initial pressure deformation starts around the outer ellipse, the pressure is exposed to the strong m/n=1/2 flows in the course of time evolution, as is observed in Fig.8. We observed that the poloidal vortices advect and deform the pressure. Consequently, the mushroom-like structure of the pressure is formed on a poloidal section. Note that we have conducted the pressure-budget analysis which had been shown in Ref.[6] for the full-torus simulations and verified that the deformation process is fully dominated by the advection. It makes a clear contrast to the half-pitch simulations in which other processes such as the fluid compression, thermal diffusion and viscous heating work to suppress deformation by the advection. It is also interesting that we observe the mushroom-like structure of the pressure because it is typically observed in inertial-fusion system. Instead of the baroclinic torque which forms mushrooms in the laser-fusion system, strong m/n=2/1 poloidal flow works to form the structure.

In our simulation, the central beta is reduced from 4.0 to 2.0 at the final time. However, the total thermal energy does not decrease so much thanks to the well-confined magnetic surfaces.

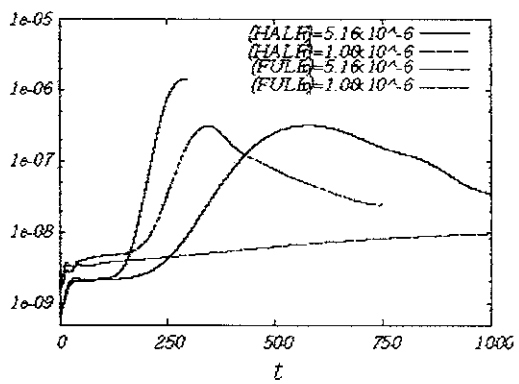

Fig.6 Time evolution of the kinetic energy per unit volume. The solid (dashed) lines represent runs for the higher (lower) resistivy. Thick (thin) lines are for the full-torus (half-pitch) simulations.

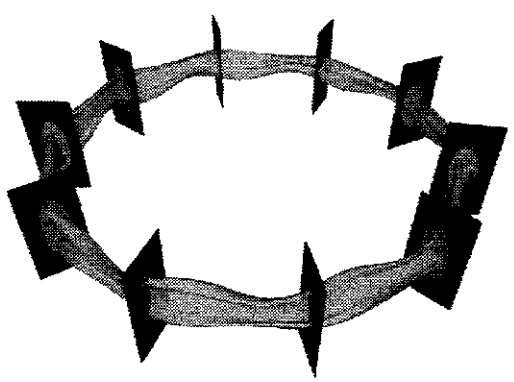

Fig.7 Isosurface of the pressure for full-torus simulation with the lower resistivity. Clear m/n=2/1 deformations are observed.

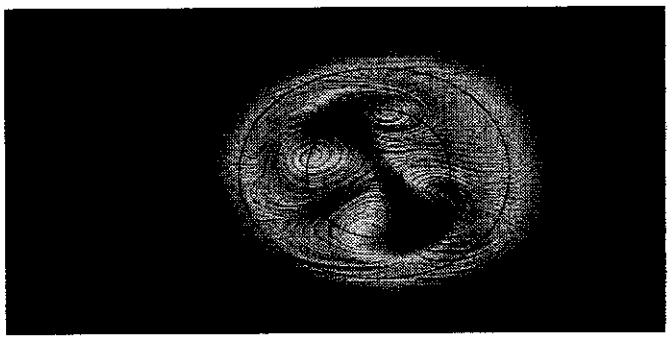

Fig.8 Color contours of the pressure on a horizontally-elongated poloidal section for the full-torus simulation with the lower resistivity at the saturation time of the kinetic energy.
Streamlines are drawn with poloidal components of the velocity field.

Acknowledgements

We acknowledge Drs. F. Paoletti, S. Sabbagh, and S. Kaye for useful discussions and providing us with the reconstructed NSTX equilibrium data.

References

[1] T. Hayashi, et al., Nucl. Fusion 40, 721, (2000); N.Mizuguchi., T.Hayashi., and T.Sato., Phys. Plasmas, 7 (2000) 940.

[2] Y. Nagayama, et al., Phys. Fluids B 5, 2571, (1993).

[3] T. Hayashi, et al., Contrib. Plasma Phys., Vol.42, No.2-4 (2002) 309-320; H. Harafuji, T. Hayashi and T. Sato, J. Comp. Phys. **81** (1989) 169.

[4]R. Kanno, N. Nakajima, T. Hayashi, and M. Okamoto, J. Plasma Fusion Res. SERIES **3** (2000) 584. ; R. Kanno, N. Nakajima, T. Hayashi, and M. Okamoto, Contrib. Plasma Phys. **40** (2000) 260.

[5]A. Komori, N. Ohyabu, et al, Plasma Physics and Controlled Nuclear Fusion Research, (Vienna, 1994), **II** (1995) 773.

[6]H. Miura, T. Hayashi and T. Sato, Phys. Plasmas **8** (2001) 4870.